PCCP

PAPER

View Article Online
View Journal | View Issue

Cite this: *Phys. Chem. Chem. Phys.*, 2018, **20**, 17497

Ab initio identification of the Li-rich phase in $LiFePO_4$†

Hua Zeng, Yue Gu, Gaofeng Teng, Yimeng Liu, Jiaxin Zheng* and Feng Pan *

Received 26th March 2018,
Accepted 4th June 2018

DOI: 10.1039/c8cp01949e

rsc.li/pccp

A recent discovery of anionic redox activity in Li-rich layered compounds opens a new direction for the design of high-capacity cathode materials for lithium-ion batteries. Here using extensive *ab initio* calculations, the thermodynamic existence of the Li-rich phase in $LiFePO_4$ to form $Li_{1+x}Fe_{1-x}PO_4$ with x not exceeding 12.5% has been proved. Anionic redox activity and structural stability during delithiation are further investigated. Interestingly, it is found that $Li_{1+x}Fe_{1-x}PO_4$ cannot be delithiated completely and thus cannot achieve extra capacity by anionic redox activity, because the local oxygen-ion redox will cause the fracture of the rigid framework formed by phosphate tetrahedral polyanions. Although an extra capacity cannot be realized, the excess Li-ions at Fe sites can enhance the Li-ion diffusivity along the adjacent [010] channel and contribute to the shift from 1D to 2D/3D diffusion. This study provides a fresh perspective on olivine-type $LiFePO_4$ and offers some important clues on designing Li-rich cathode materials with high energy density.

Introduction

With the rapid development of transportation applications, including hybrid electric vehicles, plug-in hybrid electric vehicles (PEVs) and pure electric vehicles (EVs), batteries with high energy density are urgently required.[1,2] Developing anode and cathode materials with high energy density for rechargeable lithium-ion batteries (LIBs) becomes the most important way to meet such requirements.[3] LIB anodes, such as a new graphene allotrope known as graphenylene,[4] heteroatom-doped graphene,[5] and a compound of highly dispersed nano structured carbon nanotubes (CNTs), graphene nanoplatelet (GNP) flakes and carbon nanofibers (CNFs),[6] have been found to be capable of storing lithium with higher energy density. For LIB cathode materials, traditional cathode materials have relied on cationic redox reactions, and transition metals (TM) have been considered as the sole source of electrochemical activity in an intercalation cathode to provide the charge-compensating electrons after Li-ion extraction.[7–11] As a consequence, the theoretical specific capacity is limited by the number of electrons that the TM ions can exchange per unit mass. Recently, with the discovery of anionic redox activity in Li-rich layered compounds, a new design paradigm for LIB cathodes based on a cumulative cationic and anionic redox activity has attracted increasing interest.[12–14] The anionic redox activity will create extra capacity beyond the theoretical TM redox capacity at a high voltage, thus extending the design of new high-capacity cathodes. Previously reported anionic redox activities were mainly observed within the Li-excess layered TM oxides, such as layered NMC (Ni–Mn–Co),[15–17] Li_2MnO_3,[18–20] $Li_{1.2}Ni_{0.2}Mn_{0.6}O_2$,[21] $Li_{1.3}Nb_{0.3}Me_{0.4}O_2$ (Me = Fe^{3+}, Mn^{3+} and V^{3+}),[22,23] $Li_2Ru_{1-y}Sn_yO_3$,[24,25] Li_4FeSbO_6,[26] Li_8ZrO_6,[27] α-Li_2IrO_3,[28] β-Li_2IrO_3,[29] and Li_3IrO_4.[30]

One critical issue of the practical application for the reported Li-rich layered materials is capacity fading during electrochemical cycles, due to the irreversible loss of lattice oxygen during the anionic redox process.[31,32] It will be interesting to know whether there is a possibility of forming the Li-rich phase in polyanionic intercalation TM compounds (*e.g.*, $LiFePO_4$ and Li_2FeSiO_4), as the strong P–O and Si–O covalence can stabilize the lattice oxygen during the anionic redox process. A Li-rich solid solution of $Li_{2+2x}Fe_{1-x}SiO_4$ ($0 \leq x \leq 0.3$) has been reported recently,[33] but the presence of additional Li-ions are in interstitial sites, which are different from the Li-rich layered materials with additional Li-ions occupying the TM sites. Moreover, no extra capacity in $Li_{2+2x}Fe_{1-x}SiO_4$ is reported. Actually, Li_2FeSiO_4 itself can be regarded as a kind of material with anionic redox activity, as during the delithiation of the second Li-ion, oxygen redox occurs.[34] In the crystal structure of $LiFePO_4$ (LFP), an important commercialized cathode material for rechargeable LIBs,[35–37] all of the oxygen-ions form strong covalent bonds with phosphorus to form a phosphate tetrahedral polyanion and generate a stable three-dimensional framework.[38] If the Li-rich phase exists, better structural stability compared with the reported Li-rich layered materials would be anticipated when the anionic redox occurs,

School of Advanced Materials, Peking University, Shenzhen Graduate School, Shenzhen 518055, People's Republic of China. E-mail: zhengjx@pkusz.edu.cn, panfeng@pkusz.edu.cn

† Electronic supplementary information (ESI) available. See DOI: 10.1039/c8cp01949e

thus leading to stable extra reversible lithium storage capacity beyond the theoretical value of LFP. Though the Li-excess $Li_{1.05}Fe_{0.95}PO_4$ has been recently synthesized,[39] it mainly focuses on the influence of the excess Li-ions (at Fe sites) on the Li–Fe anti-site defects and does not pay attention to the possibility of the appearance of anionic redox activity.

In this work, using extensive *ab initio* calculations, we have proved the thermodynamic existence of $Li_{1+x}Fe_{1-x}PO_4$ ($0 \leq x \leq 12.5\%$). Interestingly, the extra capacity beyond the theoretical value of LFP cannot be achieved by the Li-rich phase, due to the structural instability when the content of the extracted Li-ions exceeds $(1 - 2x)$. Further analysis reveals that the structural instability can be attributed to the fact that the local oxygen-ion redox will cause the fracture of the rigid framework formed by phosphate tetrahedral polyanions. Nevertheless, the Li-ion diffusivity in $Li_{1+x}Fe_{1-x}PO_4$ can be enhanced by the excess Li-ions at Fe sites, reflected by the reduced energy barrier for the Li-ion diffusion along the adjacent [010] channel and the shift from 1D to 2D/3D diffusion. Our findings provide a fresh perspective on olivine-type $LiFePO_4$ and offer some important clues on designing Li-rich cathode materials with high energy density.

Calculation method

All calculations were performed using the plane-wave projector-augmented wave method, as implemented in the Vienna *Ab Initio* Simulation Package (VASP). The Perdew–Burke–Ernzerhof (PBE) form of generalized gradient approximation (GGA) was chosen as the exchange–correlation potential.[40] Taking account of the strong on-site Coulomb interaction (U) presented in the localized 3d electrons of Fe, the PBE+U approach was employed with the U value set to 5.3 eV in $Li_{1+x}Fe_{1-x}PO_4$.[41,42]

Geometry optimizations and total energy calculations were spin-polarized, using a plane-wave cutoff of 520 eV. A ferromagnetic high-spin Fe state was assumed, and the energetic effects of the magnetic ordering were small (<0.04 eV). All the atomic positions and cell parameters were fully relaxed using a conjugate gradient algorithm, until the force on each atom was smaller than 0.01 eV $Å^{-1}$, and energies were converged to within 10^{-5} eV per atom. A $4 \times 3 \times 4$ k-point grid within the Monkhorst–Pack scheme was used to sample the Brillouin zone of the $Li_{1+x}Fe_{1-x}PO_4$ supercell. The supercell containing $1 \times 2 \times 2$ unit cells (space group *Pnma*) was used, which corresponded to 112 atoms per cell.

A climbing-image nudged elastic band (cNEB) method was used to calculate the energy barriers for Li-ion diffusion in the bulk $Li_{1+x}Fe_{1-x}PO_4$. The nudged elastic band (NEB) is a method for finding the saddle point and minimum energy path between the known initial state and final state. This method works by optimizing a number of intermediate images along the path. Each image finds the lowest energy possible while maintaining equal spacing to neighboring images. The cNEB method is a small modification of the NEB method in which the highest energy image is driven up to the saddle point. This image does not feel the spring forces along the band. Instead, the true force at this image along the tangent is inverted. In this way, the image tries to maximize its energy along the band, and minimize in all other directions. When this image converges, it will be at the exact saddle point.[43] The initial state is a configuration with a Li-vacancy at one of the octahedral sites and a Li-ion at the adjacent octahedral site. The final state is opposite to the initial state. Five intermediate states are inserted. All ions were relaxed for calculations of the minimum energy pathways.

Density functional perturbation theory (DFPT) was used for phonon calculations.[44] All the atomic positions were fully relaxed until the force on each atom was smaller than 0.001 eV $Å^{-1}$, and energies were converged to within 10^{-8} eV per atom. Phonopy was used to handle force constants gained by DFPT.

Results and discussion

The existence of the Li-rich phase in $LiFePO_4$

Fig. 1a shows the crystal structure of olivine-type $LiFePO_4$. It was reported to crystallize in the orthorhombic space group *Pnma* with $a = 10.3377$, $b = 6.0112$, and $c = 4.6950$ Å.[45] Correspondingly, for the $1 \times 2 \times 2$ supercell, a, b, and c should be 10.3377, 12.0224, and 9.390 Å, respectively. As shown in Table 1, the calculated lattice parameters of $LiFePO_4$ are $a = 10.447$, $b = 12.170$ and $c = 9.507$ Å, in satisfactory agreement with the experimental values. We constructed the initial structures of $Li_{1+x}Fe_{1-x}PO_4$ (x = 6.25% and 12.5%) by replacing Fe-ions with Li-ions. In $LiFePO_4$, all Fe-ions are coordinated with six oxygen-ions to form the FeO_6 octahedra, which are connected by sharing O corners to form a 2D network in the bc plane. All Fe sites are equivalent, and thus there is only one doping structure when x is 6.25% (Fig. 1b). For $x = 12.5\%$, there are a lot of doping structures. By comparing their total energies, we chose the structure with the minimum total energy for further studies. All structures of $Li_{1+x}Fe_{1-x}PO_4$ ($x = 12.5\%$) are displayed in Fig. S1 (ESI†). The structure of $Li_{1+x}Fe_{1-x}PO_4$ ($x = 18.75\%$) is displayed in Fig. S2 (ESI†).

Table 1 shows the variation of lattice parameters and the volume of $Li_{1+x}Fe_{1-x}PO_4$ after structural optimization. With the

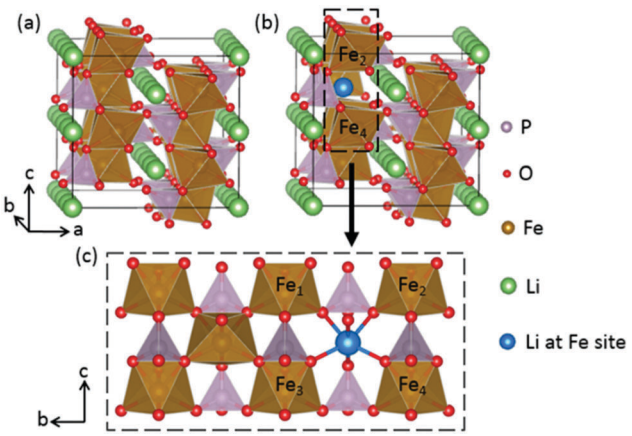

Fig. 1 (a) Schematic for the structure of $LiFePO_4$. (b) Schematic for the structure of $Li_{1+x}Fe_{1-x}PO_4$ ($x = 6.25\%$). (c) The structure configuration around the excess Li-ion at the Fe site in the bc plane (without considering Li-ions in the [010] channel).

Table 1 The variation of lattice parameters, volume and calculated formation energy of $Li_{1+x}Fe_{1-x}PO_4$

x	a [Å]	b [Å]	c [Å]	α [°]	β [°]	γ [°]	V [Å^3]	ΔH_f [eV per f.u.]
0	10.447	12.170	9.507	90.00	90.00	90.00	1208.77	−12.488
6.25%	10.420	12.146	9.504	90.00	90.11	90.00	1202.81	−12.677
12.5%	10.380	12.128	9.508	90.00	90.13	90.00	1196.98	−12.908
18.75%	10.366	12.083	9.506	90.00	90.30	90.00	1190.71	−13.130

increase of x, a and b lattices shrink slightly, c remains nearly invariant, and the volume gets smaller as well. Moreover, the excess Li-ions at Fe sites change the structural symmetry, resulting in a slight structural tilt with the β angle exceeding 90°.

To study the thermodynamic stability of $Li_{1+x}Fe_{1-x}PO_4$, we first calculate its formation energy (enthalpy), ΔH_f ($Li_{1+x}Fe_{1-x}PO_4$), which is defined as the total energy change of the following reaction,[46]

$$\Delta H_f = E_{tot}(Li_{1+x}Fe_{1-x}PO_4) - (1+x)E_{crystal}(Li) - (1-x)E_{crystal}(Fe) - E_{crystal}(P) - 2E_{gas}(O_2) \quad (1)$$

where E_{tot} ($Li_{1+x}Fe_{1-x}PO_4$) is the total energy of $Li_{1+x}Fe_{1-x}PO_4$, $E_{crystal}$ (Li), $E_{crystal}$ (Fe) and $E_{crystal}$ (P) are Li, Fe and P at their most stable phases, respectively, and E_{gas} (O_2) is the energy of O_2 molecular gas. The calculated formation energies of different x values are shown in Table 1. We can see that ΔH_f ($Li_{1+x}Fe_{1-x}PO_4$) decreases with the increase of x and it is less than zero, indicating that $Li_{1+x}Fe_{1-x}PO_4$ is stable.

Phonons play an important role in dynamic behaviors and thermal properties. Using first-principles phonon calculations,[44] the phonon band structures of $Li_{1+x}Fe_{1-x}PO_4$ are obtained. As shown in Fig. 2a, there is no imaginary frequency in the phonon band structure of $LiFePO_4$, in accordance with the cognition that $LiFePO_4$ is thermodynamically stable. Imaginary frequency also doesn't appear in $Li_{1+x}Fe_{1-x}PO_4$ with x = 6.25% and 12.5% (Fig. 2b and c), which further proves that $Li_{1+x}Fe_{1-x}PO_4$ (x = 6.25% and 12.5%) are thermodynamically stable. By contrast, the phonon band structure of $Li_{1+x}Fe_{1-x}PO_4$ (x = 18.75%) shows imaginary frequency (Fig. 2d), which seems to contradict the result of formation energy. In fact, the formation energy is a thermal index, but the phonon band structure is a lattice dynamic index. Here, the structure conforming to the two indexes is truly thermodynamically stable. From this perspective, with the increasing content of Li-ions occupying Fe sites, there is a limit for the x value to ensure the structural stability of $Li_{1+x}Fe_{1-x}PO_4$.

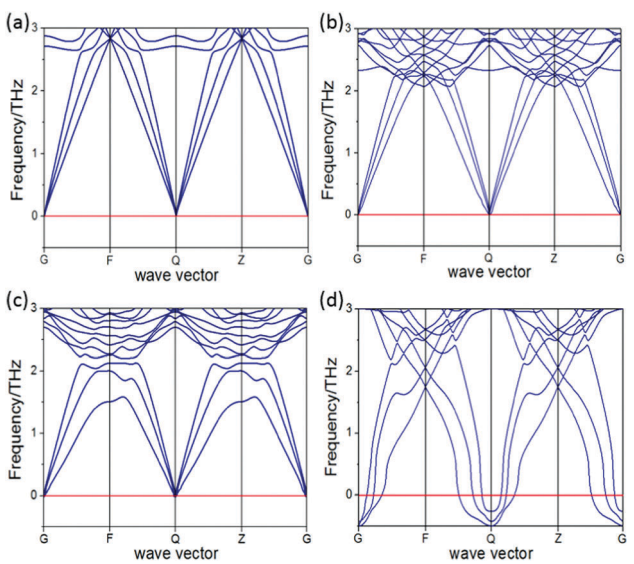

Fig. 2 Phonon band structures of $Li_{1+x}Fe_{1-x}PO_4$. (a) x = 0; (b) x = 6.25%; (c) x = 12.5%; (d) x = 18.75%. Above the red line is real frequency, and below the red line is imaginary frequency.

Can the Li-rich phase introduce extra capacity?

Whether Li-rich phase $Li_{1+x}Fe_{1-x}PO_4$ is able to achieve extra capacity beyond the theoretical value of $LiFePO_4$ is an important issue we care about. The extra capacity depends on the maximum amount of Li-ions that can be extracted (also the transferable electrons). Hence, the structural stability after delithiation of $Li_{1+x}Fe_{1-x}PO_4$ is further studied. Fig. 3 shows the phonon band structures of $Li_{1+x-y}Fe_{1-x}PO_4$ (x = 6.25%, $y = 1-2x$, 1, and $1+x$). It can be seen that the structure is stable when $y = 1-2x$ (all Fe-ions are in the +3 oxidation state), but unstable when $y > 1-2x$.

In addition, we also performed molecular dynamics simulations to verify the instability of $Fe_{1-x}PO_4$ (x = 6.25% and 12.5%). Fig. S3 (ESI†) provides the initial and final atomic configurations

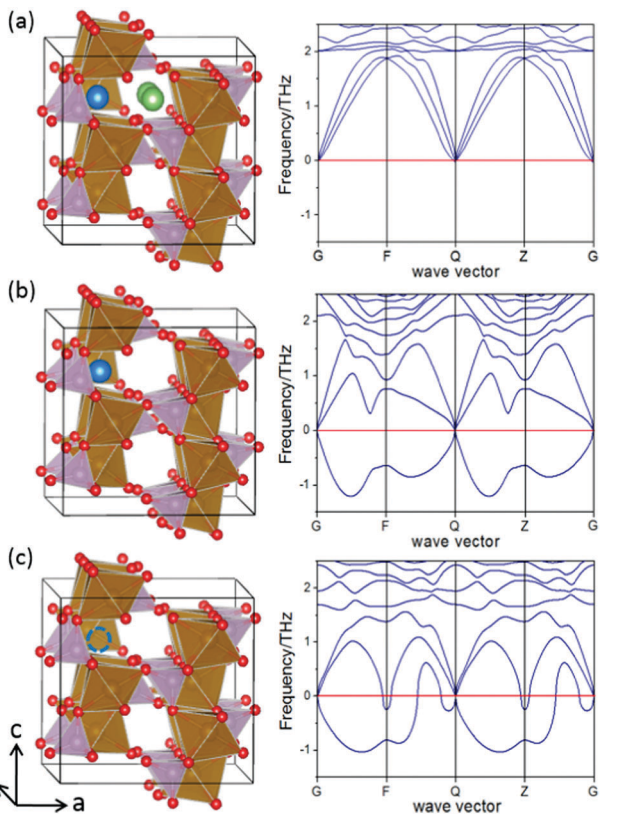

Fig. 3 Schematics for structures of $Li_{1+x-y}Fe_{1-x}PO_4$ (x = 6.25%) with increasing content of delithiation and the corresponding phonon band structures. (a) $y = 1-2x$; (b) y = 1; (c) $y = 1+x$. Above the red line is real frequency, and below the red line is imaginary frequency.

obtained at times of 0 and 3 ps at room temperature (300 K). It is obvious that some Fe-ions deviate from the original positions and the distances between the Fe-ions and their neighboring oxygen-ions become too large (3.5 Å) to form Fe–O bonds (the Fe–O bond lengths in $LiFePO_4$ don't exceed 2.3 Å). The above results suggest that $Li_{1+x}Fe_{1-x}PO_4$ (x = 6.25% and 12.5%) cannot be delithiated completely, and thus cannot enhance the specific capacity of $LiFePO_4$. This is different from our intuitive wish that the $Li_{1+x}Fe_{1-x}PO_4$ would introduce extra capacity for lithium storage, due to the good stability of the rigid polyanion framework with strong P–O covalence. We investigated the detailed reasons why the Li-rich phase in $LiFePO_4$ cannot introduce extra capacity by the change in the valence state of elements.

In $Li_{1+x}Fe_{1-x}PO_4$ (x = 6.25% and 12.5%), some Fe sites are occupied by Li-ions, so the valence state of Fe must change due to charge compensation, which is confirmed by analyzing the projected electronic density of states (PDOS) of $Li_{1+x}Fe_{1-x}PO_4$. Fig. 4a shows the PDOS of $LiFePO_4$. By integrating the Fe 3d state (spin up and spin down) below the Fermi level, we can calculate that the magnetic moments of all Fe-ions are 3.74 μ_B, consistent with the fact that the Fe-ions are in the +2 oxidation state and exhibit a high spin $t_{2g}(\downarrow)t_{2g}^3(\uparrow)e_g^2(\uparrow)$ configuration in $LiFePO_4$.[47] Fig. S4a (ESI†) shows the PDOS of $FePO_4$. The magnetic moments of all Fe-ions are 4.31 μ_B, consistent with the fact that the Fe-ions are in the +3 oxidation state and exhibit a high spin $t_{2g}^3(\uparrow)e_g^2(\uparrow)$ configuration in $FePO_4$. Comparing Fig. 4a–c, we can see that with the increase of x, the Fe 3d state (spin down) gradually crosses the Fermi level, indicating that some Fe^{2+} ions are oxidized to the Fe^{3+} state. We also calculated the magnetic moments of different Fe-ions around the excess Li-ions at the Fe site in the cases when x = 6.25% and 12.5% (Fig. 1c). When x is 6.25%, the magnetic moments of Fe_1, Fe_2, Fe_3 and Fe_4 are 3.74, 3.74, 4.07 and 4.07 μ_B, respectively. Interestingly, Fe_3 and Fe_4 have been oxidized but not fully to Fe^{3+}. When x is 12.5%, the magnetic moments of Fe_1, Fe_2, Fe_3 and Fe_4 are 3.74, 3.74, 4.31 and 4.31 μ_B, respectively. Obviously, Fe_3 and Fe_4 are fully oxidized to Fe^{3+}. Both at x = 6.25% and 12.5%, the oxidized Fe-ions are Fe_3 and Fe_4, and not Fe_1 and Fe_2, which can also be reflected by the shorter Fe–O bond for Fe_3 and Fe_4 in Table S1 (ESI†).

Furthermore, we calculate the PDOS of $Li_{1+x-y}Fe_{1-x}PO_4$ (x = 6.25% and 12.5%). As shown in Fig. S4 (ESI†), when the content of the extracted Li-ions approaches $(1 - 2x)$, the Fe 3d state (spin down) fully crosses the Fermi level, meaning that all Fe^{2+} ions are oxidized to Fe^{3+}. When the content of the extracted Li-ions approaches $(1 + x)$, namely $Fe_{1-x}PO_4$, the O 2p state (spin up) gradually crosses the Fermi level, which means that some O-ions begin to oxidize. Note that Fig. S4 (ESI†) is used to illustrate how the valence state of different elements change during the delithiation of $Li_{1+x}Fe_{1-x}PO_4$, which are related to the PDOS near the Fermi level. As shown in Fig. S5 (ESI†), during the delithiation of $Li_{1+x}Fe_{1-x}PO_4$ (x = 6.25%), the PDOS of P and Li atoms are far from the Fermi level and remain nearly unchanged. Hence, we only care about the contributions of the PDOS of Fe and O when analyzing the redox process. Fig. 5 shows the PDOS of O 2p orbitals of four different oxygen-ion

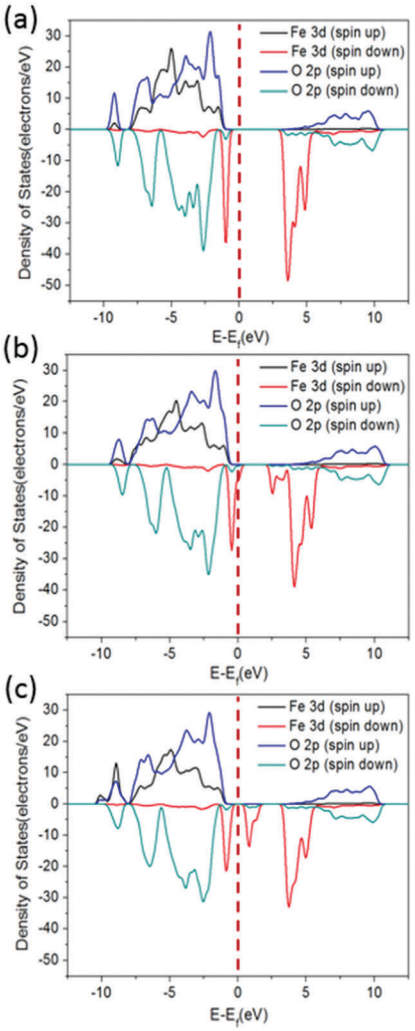

Fig. 4 The PDOS of $Li_{1+x}Fe_{1-x}PO_4$. (a) x = 0; (b) x = 6.25%; (c) x = 12.5%. The Fermi level (the vertical red dashed line) is set to zero energy.

environments in $Fe_{1-x}PO_4$ (x = 6.25%). It can be seen clearly that O_c and O_d are oxidized, which are the O-ions bonding with the Li-ion at the Fe site in $Li_{1+x}Fe_{1-x}PO_4$. So if $Li_{1+x-y}Fe_{1-x}PO_4$ ($y > 1 - 2x$) existed stably, Fe-ions would remain in the +3 oxidation state, and the O-ions around the Li-vacancy at the Fe site would be oxidized. The local O-ion redox would result in the fracture of the rigid framework formed by phosphate tetrahedral polyanions. This inference coincides with the above calculated phonon band structures.

In order to understand the structural instability caused by the local O-ion oxidation easily, we compared the structural distortion during delithiation. In $LiFePO_4$, FeO_6 octahedra are connected by sharing O corners to form a 2D network in the *bc* plane, and the PO_4 tetrahedrons act as joints to connect adjacent FeO_6 2D layers. The FeO_6 octahedra tend to be distorted during the cationic and anionic redox, which will also lead to the shrinkage of FeO_6 2D layers, but the PO_4 tetrahedrons between the FeO_6 2D layers would prevent this distortion and shrinkage due to the strong P–O covalence. During the transition from $LiFePO_4$ to $FePO_4$ (Fig. 6a), the length of the Fe–O bonds shortens and lattice a shrinks by

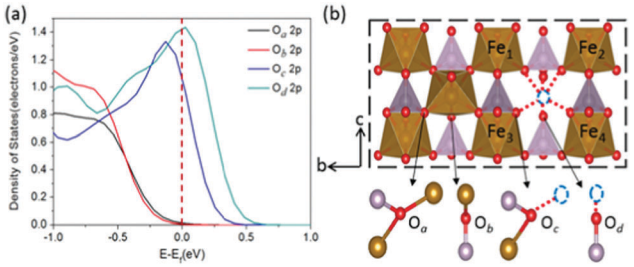

Fig. 5 (a) The PDOS of O 2p orbitals of four different oxygen-ion environments in $Fe_{1-x}PO_4$ (x = 6.25%). (b) The corresponding structure configurations of oxygen coordinated by Fe/P. In $FePO_4$, there are two kinds of oxygen-ion environments: O_a is coordinated by 2 Fe and 1 P, O_b is coordinated by 1 Fe and 1 P. In $Fe_{1-x}PO_4$, O_a transforms into O_c, and O_b transforms into O_d around the Li-vacancy at the Fe site.

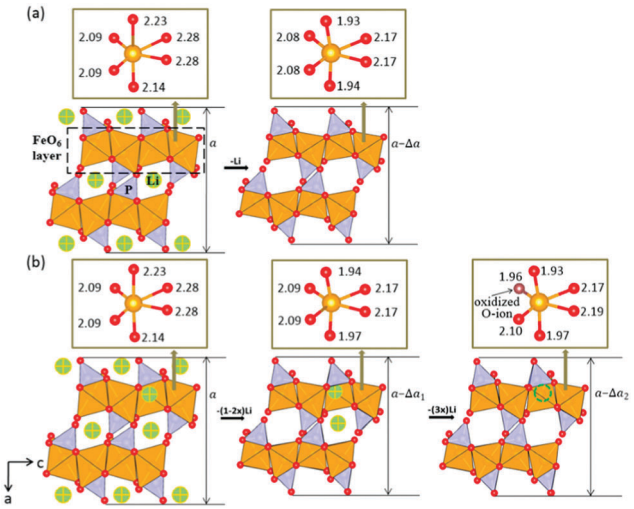

Fig. 6 Fully relaxed configuration for (a) $LiFePO_4$ and $FePO_4$; (b) $Li_{1+x}Fe_{1-x}PO_4$, $Li_{3x}Fe_{1-x}PO_4$ and $Fe_{1-x}PO_4$. The unit of all bond lengths is Å.

4.36% (Table 2). This process is essentially a phase transition.[48] For the Li-rich phase $Li_{1+x}Fe_{1-x}PO_4$, from $Li_{1+x}Fe_{1-x}PO_4$ to $Li_{3x}Fe_{1-x}PO_4$ (x = 6.25%) with only Fe^{2+}/Fe^{3+} redox (Fig. 6b), lattice a shrinks by 3.98% and the change in length of Fe–O bonds in the FeO_6 octahedra is similar to the phase transition from $LiFePO_4$ to $FePO_4$. However, during the oxygen-ion redox from $Li_{3x}Fe_{1-x}PO_4$ to $Fe_{1-x}PO_4$ (x = 6.25%), lattice a shrinks only by 0.11% and the PO_4 tetrahedrons do not allow the shrinkage of FeO_6 2D layers any more. In addition, different from the process with only cationic redox, the length of the bond between Fe-ions and the oxidized O-ion shortens sharply during the anionic redox, indicating another kind of phase transition aggravating the structure of $Fe_{1-x}PO_4$, leading to the fracture of the pretty rigid frame structure of phosphate tetrahedral polyanions. Thus, $Li_{1+x}Fe_{1-x}PO_4$ cannot be delithiated completely, and cannot introduce extra capacity beyond the theoretical value of $LiFePO_4$.

Table 2 The calculated specific change of $LiFePO_4$ and $Li_{1+x}Fe_{1-x}PO_4$ (x = 6.25%) during delithiation

	Δa [a]		Δa [a]
$LiFePO_4$	0	$Li_{1+x}Fe_{1-x}PO_4$	0
$FePO_4$	4.36%	$Li_{3x}Fe_{1-x}PO_4$	3.98%
		$Fe_{1-x}PO_4$	4.09%

The enhanced Li-ion diffusivity in $Li_{1+x}Fe_{1-x}PO_4$

It is widely known that Li-ions diffuse along the [010] channel in the bulk $LiFePO_4$.[49] Li-ions hop between adjacent octahedral sites *via* a tetrahedron hollow formed by the edge-sharing LiO_6 octahedrons.[50] Similar migration trajectories exist in the bulk $Li_{1+x}Fe_{1-x}PO_4$ (x = 6.25% and 12.5%). As shown in Fig. 7a, 1 stands for a Li-ion and 2 stands for a Li-vacancy. The path 1–2 is the migration pathway of Li-ion diffusion along the [010] direction. In the bulk $LiFePO_4$, the barrier for a Li-ion to hop from the 1 site to the 2 site is 0.448 eV. This result is very close to 0.42 eV obtained by Christian Kuss.[51] In $Li_{1+x}Fe_{1-x}PO_4$ (x = 6.25% and 12.5%), the barriers for a Li-ion to hop from the 1 site to the 2 site are 0.299 and 0.416 eV (Fig. 7c), respectively, lower than the barrier at x = 0. This indicates that the excess Li-ions at Fe sites can enhance the Li-ion diffusivity along the adjacent [010] channel, coinciding with the results obtained by Kyu-Young Park.[39] The energy barriers for Li-ion diffusion along another adjacent [010] channel are shown in Fig. S6 (ESI†), exhibiting the same inference. The enhanced Li-ion diffusivity in $Li_{1+x}Fe_{1-x}PO_4$ along the adjacent [010] channels can be explained as follows: comparing the crystal structures of $LiFePO_4$ with $Li_{1+x}Fe_{1-x}PO_4$, the 0 site is occupied

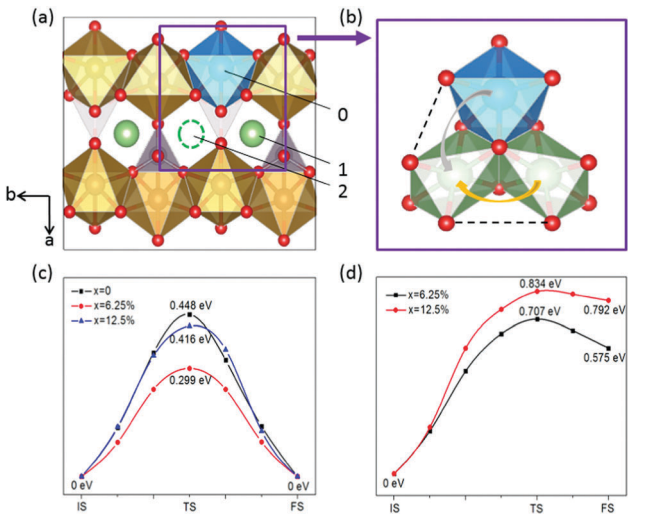

Fig. 7 (a) Schematic for the structure of $Li_{1+x}Fe_{1-x}PO_4$. 1 stands for a Li-ion and 2 stands for a Li-vacancy in the [010] channel. 0 means a Li-ion at the Fe site. (b) The migration pathway of Li-ion diffusion predicted by our calculations. The yellow arrow represents the path of Li-ion hoping from the 1 site to the 2 site, which is along the [010] direction through face-shared vacant tetrahedral sites. The gray arrow represents the path of Li-ion hoping from the 0 site to the 2 site, which is along the [110] direction through face-shared vacant tetrahedral sites. (c) The energy barriers for a Li-ion to hop from the 1 site to the 2 site in the bulk $Li_{1+x}Fe_{1-x}PO_4$ (x = 0, 6.25% and 12.5%). (d) The energy barriers for a Li-ion to hop from the 0 site to the 2 site in the bulk $Li_{1+x}Fe_{1-x}PO_4$ (x = 6.25% and 12.5%). IS, TS and FS represent the initial, transitional and final states, respectively.

by Fe-ions in $LiFePO_4$, but it is occupied by Li-ions in $Li_{1+x}Fe_{1-x}PO_4$ (x = 6.25% and 12.5%). Due to the much smaller charge of the Li-ions at the Fe site, the Coulombic repulsion between the metal-ion at the 0 site and the Li-ion at the 1/2 site decreases greatly. In addition, the distance between the 1 site and the 2 site becomes shortened after the doping of Li-ions at Fe sites (Table S2, ESI†).

Besides that, we calculated the diffusion barrier for Li-ion hopping from the 0 site to the 2 site in the bulk $Li_{1+x}Fe_{1-x}PO_4$ (x = 6.25% and 12.5%). As shown in Fig. 7d, the energy barriers are 0.707 and 0.834 eV, respectively, a little higher than the calculated result of path 1–2, but much lower than 3.36 eV,[52] which is the energy barrier for Li-ion diffusion along the [101] direction in the bulk $LiFePO_4$. GKP Dathar pointed that when Li–Fe anti-site defects arose in $LiFePO_4$, the energy barrier for a Li-ion to hop from the Fe site to the Li site in the adjacent [010] channel varied in the range of 0.75–0.85 eV.[53] Malik *et al.* proved that Li-ions could cross over between different [010] channels and the diffusion mechanism tended to shift from 1D to 2D/3D in the presence of a large concentration of anti-site defects.[54] Therefore, we can see clearly that the Li-ion at the 0 site has the ability to transfer to the 2 site, activating the shift from 1D to 2D/3D diffusion. Fig. 7b summarizes the migration pathway of Li-ion diffusion predicted by our calculations. Similar to the migration pathway of Li-ion diffusion along the [010] channel (yellow arrow), Li-ions at the Fe site hop from the Fe site to the Li site in the adjacent [010] channel *via* a tetrahedron hollow formed by the edge-sharing LiO_6 octahedra (gray arrow).

Conclusions

In summary, this work presents a systematic theoretical study of the Li-rich olivine phase in $LiFePO_4$. Our calculated results show that $Li_{1+x}Fe_{1-x}PO_4$ are thermodynamically stable when x does not exceed 12.5%. $Li_{1+x}Fe_{1-x}PO_4$ cannot achieve the extra capacity by anionic redox activity, because the structure becomes unstable when the content of the extracted Li-ions exceeds $(1 - 2x)$. This can be attributed to the fact that the local oxygen-ion redox will cause the fracture of the rigid frame structure formed by phosphate tetrahedral polyanions. Though the extra capacity cannot be achieved in $Li_{1+x}Fe_{1-x}PO_4$, the Li-ion diffusivity is enhanced by the excess Li-ions at Fe sites, reflected by the reduced energy barrier for the Li-ion diffusion along the adjacent [010] channel and the shift from 1D to 2D/3D diffusion. Our findings provide a fresh perspective on olivine-type $LiFePO_4$ and offer some important clues on designing Li-rich cathode materials with high energy density.

Conflicts of interest

There are no conflicts to declare.

Acknowledgements

This work was financially supported by the National Materials Genome Project (2016YFB0700600), the National Natural Science Foundation of China (No. 21603007 and 51672012), and the Shenzhen Science and Technology Research Grant (No. JCYJ20150729111733470 and JCYJ20151015162256516).

Notes and references

1 B. Dunn, H. Kamath and J.-M. Tarascon, *Science*, 2011, **334**, 928–935.
2 C. Masquelier and L. Croguennec, *Chem. Rev.*, 2013, **113**, 6552–6591.
3 J. Lu, Z. Chen, Z. Ma, F. Pan, L. A. Curtiss and K. Amine, *Nat. Nanotechnol.*, 2016, **11**, 1031–1038.
4 Y.-X. Yu, *J. Mater. Chem. A*, 2013, **1**, 13559–13566.
5 Y.-X. Yu, *Phys. Chem. Chem. Phys.*, 2013, **15**, 16819–16827.
6 N. Badi, *J. Mater. Sci.: Mater. Electron.*, 2016, **27**, 10342–10346.
7 J. B. Goodenough and Y. Kim, *Chem. Mater.*, 2009, **22**, 587–603.
8 Z. Lu, D. MacNeil and J. Dahn, *Electrochem. Solid-State Lett.*, 2001, **4**, A191–A194.
9 T. Ohzuku, A. Ueda, M. Nagayama, Y. Iwakoshi and H. Komori, *Electrochim. Acta*, 1993, **38**, 1159–1167.
10 H. Ren, Y. Huang, Y. Wang, Z. Li, P. Cai, Z. Peng and Y. Zhou, *Mater. Chem. Phys.*, 2009, **117**, 41–45.
11 K. Mizushima, P. Jones, P. Wiseman and J. B. Goodenough, *Mater. Res. Bull.*, 1980, **15**, 783–789.
12 D. H. Seo, J. Lee, A. Urban, R. Malik, S. Kang and G. Ceder, *Nat. Chem.*, 2016, **8**, 692–697.
13 M. Saubanère, E. McCalla, J. M. Tarascon and M. L. Doublet, *Energy Environ. Sci.*, 2016, **9**, 984–991.
14 Y. Xie, M. Saubanère and M. L. Doublet, *Energy Environ. Sci.*, 2017, **10**, 266–274.
15 H. Koga, L. Croguennec, M. Ménétrier, K. Douhil, S. Belin, L. Bourgeois, E. Suard, F. Weill and C. Delmas, *J. Electrochem. Soc.*, 2013, **160**, A786–A792.
16 M. Oishi, C. Yogi, I. Watanabe, T. Ohta, Y. Orikasa, Y. Uchimoto and Z. Ogumi, *J. Power Sources*, 2015, **276**, 89–94.
17 K. Luo, M. R. Roberts, R. Hao, N. Guerrini, D. M. Pickup, Y.-S. Liu, K. Edström, J. Guo, A. V. Chadwick, L. C. Duda and P. G. Bruce, *Nat. Chem.*, 2016, **8**, 684–691.
18 H. Chen and M. S. Islam, *Chem. Mater.*, 2016, **28**, 6656–6663.
19 R. Xiao, H. Li and L. Chen, *Chem. Mater.*, 2012, **24**, 4242–4251.
20 M. Oishi, K. Yamanaka, I. Watanabe, K. Shimoda, T. Matsunaga, H. Arai, Y. Ukyo, Y. Uchimoto, Z. Ogumi and T. Ohta, *J. Mater. Chem. A*, 2016, **4**, 9293–9302.
21 K. Luo, M. R. Roberts, N. Guerrini, N. Tapia-Ruiz, R. Hao, F. Massel, D. M. Pickup, S. Ramos, Y.-S. Liu, J. Guo, A. V. Chadwick, L. C. Duda and P. G. Bruce, *J. Am. Chem. Soc.*, 2016, **138**, 11211–11218.
22 N. Yabuuchi, M. Takeuchi, M. Nakayama, H. Shiiba, M. Ogawa, K. Nakayama, T. Ohta, D. Endo, T. Ozaki and T. Inamasu, *Proc. Natl. Acad. Sci. U. S. A.*, 2015, **112**, 7650–7655.
23 N. Yabuuchi, M. Nakayama, M. Takeuchi, S. Komaba, Y. Hashimoto, T. Mukai, H. Shiiba, K. Sato, Y. Kobayashi and A. Nakao, *Nat. Commun.*, 2016, **7**, 13814.
24 M. Sathiya, G. Rousse, K. Ramesha, C. Laisa, H. Vezin, M. T. Sougrati, M. Doublet, D. Foix, D. Gonbeau and W. Walker, *Nat. Mater.*, 2013, **12**, 827.

25 M. Sathiya, J.-B. Leriche, E. Salager, D. Gourier, J.-M. Tarascon and H. Vezin, *Nat. Commun.*, 2015, **6**, 6276.
26 E. McCalla, M. T. Sougrati, G. Rousse, E. J. Berg, A. Abakumov, N. Recham, K. Ramesha, M. Sathiya, R. Dominko and G. Van Tendeloo, *J. Am. Chem. Soc.*, 2015, **137**, 4804–4814.
27 S. Huang, B. E. Wilson, B. Wang, Y. Fang, K. Buffington, A. Stein and D. G. Truhlar, *J. Am. Chem. Soc.*, 2015, **137**, 10992–11003.
28 E. McCalla, A. M. Abakumov, M. Saubanère, D. Foix, E. J. Berg, G. Rousse, M.-L. Doublet, D. Gonbeau, P. Novák and G. Van Tendeloo, *Science*, 2015, **350**, 1516–1521.
29 P. E. Pearce, A. J. Perez, G. Rousse, M. Saubanère, D. Batuk, D. Foix, E. McCalla, A. M. Abakumov, G. Van Tendeloo, M.-L. Doublet and J. M. Tarascon, *Nat. Mater.*, 2017, **16**, 580–586.
30 A. J. Perez, Q. Jacquet, D. Batuk, A. Iadecola, M. Saubanère, G. Rousse, D. Larcher, H. Vezin, M.-L. Doublet and J.-M. Tarascon, *Nat. Energy*, 2017, **2**, 954.
31 J. R. Croy, M. Balasubramanian, K. G. Gallagher and A. K. Burrell, *Acc. Chem. Res.*, 2015, **48**, 2813–2821.
32 R. Benedek and H. Iddir, *J. Phys. Chem. C*, 2017, **121**, 6492–6499.
33 J. Billaud, C. Eames, N. Tapia-Ruiz, M. R. Roberts, A. J. Naylor, A. R. Armstrong, M. S. Islam and P. G. Bruce, *Adv. Energy Mater.*, 2017, **7**, 1601043.
34 T. Masese, C. Tassel, Y. Orikasa, Y. Koyama, H. Arai, N. Hayashi, J. Kim, T. Mori, K. Yamamoto, Y. Kobayashi, H. Kageyama, Z. Ogumi and Y. Uchimoto, *J. Phys. Chem. C*, 2015, **119**, 10206–10211.
35 J. B. Goodenough and K. S. Park, *J. Am. Chem. Soc.*, 2013, **135**, 1167–1176.
36 J. Zheng, Y. Hou, Y. Duan, X. Song, Y. Wei, T. Liu, J. Hu, H. Guo, Z. Zhuo, L. Liu, Z. Chang, X. Wang, D. Zherebetskyy, Y. Fang, Y. Lin, K. Xu, L. W. Wang, Y. Wu and F. Pan, *Nano Lett.*, 2015, **15**, 6102–6109.
37 L.-X. Yuan, Z.-H. Wang, W.-X. Zhang, X.-L. Hu, J.-T. Chen, Y.-H. Huang and J. B. Goodenough, *Energy Environ. Sci.*, 2011, **4**, 269–284.
38 A. Yamada, M. Hosoya, S.-C. Chung, Y. Kudo, K. Hinokuma, K.-Y. Liu and Y. Nishi, *J. Power Sources*, 2003, **119-121**, 232–238.
39 K.-Y. Park, I. Park, H. Kim, G. Yoon, H. Gwon, Y. Cho, Y. S. Yun, J.-J. Kim, S. Lee, D. Ahn, Y. Kim, H. Kim, I. Hwang, W.-S. Yoon and K. Kang, *Energy Environ. Sci.*, 2016, **9**, 2902–2915.
40 J. P. Perdew, K. Burke and M. Ernzerhof, *Phys. Rev. Lett.*, 1996, **77**, 3865–3868.
41 V. I. Anisimov, J. Zaanen and O. K. Andersen, *Phys. Rev. B: Condens. Matter Mater. Phys.*, 1991, **44**, 943–954.
42 F. Zhou, C. A. Marianetti, M. Cococcioni, D. Morgan and G. Ceder, *Phys. Rev. B: Condens. Matter Mater. Phys.*, 2004, **69**, 201101.
43 G. Henkelman, B. P. Uberuaga and H. Jonsson, *J. Chem. Phys.*, 2000, **113**, 9901–9904.
44 A. Togo and I. Tanaka, *Scr. Mater.*, 2015, **108**, 1–5.
45 G. Rousse, J. R. Carvajal, S. Patoux and C. Masquelier, *Chem. Mater.*, 2003, **15**, 4082–4090.
46 S. Chen, P. Narang, H. A. Atwater and L. W. Wang, *Adv. Mater.*, 2014, **26**, 311–315.
47 T. Maxisch, F. Zhou and G. Ceder, *Phys. Rev. B: Condens. Matter Mater. Phys.*, 2006, **73**, 104301.
48 Y. Orikasa, T. Maeda, Y. Koyama, H. Murayama, K. Fukuda, H. Tanida, H. Arai, E. Matsubara, Y. Uchimoto and Z. Ogumi, *J. Am. Chem. Soc.*, 2013, **135**, 5497–5500.
49 D. Morgan, A. Van der Ven and G. Ceder, *Electrochem. Solid-State Lett.*, 2004, **7**, A30–A32.
50 S. Nishimura, G. Kobayashi, K. Ohoyama, R. Kanno, M. Yashima and A. Yamada, *Nat. Mater.*, 2008, **7**, 707–711.
51 C. Kuss, G. Liang and S. B. Schougaard, *J. Mater. Chem.*, 2012, **22**, 24889–24893.
52 M. S. Islam, D. J. Driscoll, C. A. J. Fisher and P. R. Slater, *Chem. Mater.*, 2005, **17**, 5085–5092.
53 G. K. P. Dathar, D. Sheppard, K. J. Stevenson and G. Henkelman, *Chem. Mater.*, 2011, **23**, 4032–4037.
54 R. Malik, D. Burch, M. Bazant and G. Ceder, *Nano Lett.*, 2010, **10**, 4123–4127.